Photometric Multi-View Mesh Refinement for High-Resolution Satellite Images

Mathias Rothermel^{b,*}, Ke Gong^a, Dieter Fritsch^a, Konrad Schindler^b, Norbert Haala^a

^aInstitute for Photogrammetry, University of Stuttgart ^bPhotogrammetry and Remote Sensing, ETH Zurich

Abstract

Modern high-resolution satellite sensors collect optical imagery with ground sampling distances (GSDs) of 30-50cm, which has sparked a renewed interest in photogrammetric 3D surface reconstruction from satellite data. State-of-the-art reconstruction methods typically generate 2.5D elevation data. Here, we present an approach to recover full 3D surface meshes from multi-view satellite imagery. The proposed method takes as input a coarse initial mesh and refines it by iteratively updating all vertex positions to maximise the photo-consistency between images. Photo-consistency is measured in image space, by transferring texture from one image to another via the surface. We derive the equations to propagate changes in texture similarity through the rational function model (RFM), often also referred to as rational polynomial coefficient (RPC) model. Furthermore, we devise a hierarchical scheme to optimise the surface with gradient descent. In experiments with two different datasets, we show that the refinement improves the initial digital elevation models (DEMs) generated with conventional dense image matching. Moreover, we demonstrate that our method is able to reconstruct true 3D geometry, such as facade structures, if off-nadir views are available.

Keywords: 3D reconstruction, DSM, multi-view-stereo image matching, satellite imagery

1. Introduction

Automatic reconstruction of surface models from airborne and space-borne imagery is a long-standing problem in photogrammetry and computer vision. For imagery collected by airborne platforms, state-of-the-art algorithms allow for country-scale reconstructions with an impressive level of detail and a high degree of robustness, as demonstrated for instance by the city models now included in virtual online globes. In many applications built-up areas are most

^{*}Corresponding author

interesting and thus mapped on a regular basis, often with centimeter resolution. The most common product are still 2.5D digital surface models (DSMs) generated from airborne nadir imagery. More recent camera systems can also collect oblique views and enable the reconstruction of true 3D structures, in particular facade elements. Compared to airborne imagery, traditional satellite sensors acquired images with lower resolution, less redundancy, and only nadir views. Consequently, 2.5D DSMs are still the predominant representation for satellite-based reconstructions. The launch of new satellites with steerable high-resolution sensors, such as for instance WordView3, has led to a renewed interest in detailed reconstruction from spaceborne imagery. With these new systems, datasets with down to 0.3m GSD and high redundancy can be collected, see for example recent benchmarks [3, 44]. Given such data, the extraction of real 3D geometry, like balconies and other facade structures, seems to be in reach. Most existing algorithms, however, only produce 2.5D height maps or surfaces [35, 69, 13, 58, 23] and do not even attempt to recover 3D details.

Besides the 2.5D scene representation, conventional reconstruction pipelines have further drawbacks. They are often based on pair-wise (dense) stereo and subsequent fusion of stereo models, which does not fully exploit the multiview redundancy. Moreover, the dominant binocular stereo algorithm in those pipelines is Semi-Global Matching (SGM) [27], due to its good compromise between quality and computational cost. The price to pay is that SGM and its variants are, by construction, subject to modeling errors such as fronto-parallel bias (caused by rectangular matching windows) and a preference for areas of constant disparity [52, 54]. It is also well-documented that methods that estimate sub-pixel disparities in discrete disparity space introduce further systematic errors [59, 61, 22]. The fusion of individual stereo models into a single, consistent height field is most often done with heuristic rules, which certainly improve robustness and accuracy, but are nevertheless sub-optimal. In particular, visibility and occlusions are often handled poorly, or not at all.

To sidestep the mentioned limitations, we propose a novel reconstruction approach that uses a 3D mesh representation. Our method is a local optimisation starting from an initial mesh, i.e., it refines an existing surface model, for instance a conventional 2.5D stereo result. Following [10, 64], we assume that the coarse, initial mesh is topologically correct and we refine it by iteratively moving its vertices in the direction that most reduces the texture transfer error across all views. Technically, this is implemented as a variational energy minimisation, subject to a surface smoothness prior. Here, we formulate the corresponding energy function for the RPC model, the dominant sensor model for satellite images. We demonstrate, for the first time, the reconstruction of full 3D surface structure, by incorporating satellite views with large off-nadir angles. Moreover, we show that the refinement also tends to improve the accuracy of the 2.5D elevation values.

2. Related Work

The majority of reconstruction algorithms for optical satellite imagery employ the scheme of pairwise epipolar rectification and dense stereo matching, followed by the fusion of depth maps [35, 69, 13, 58, 23]. Epipolar rectification warps an image pair such that corresponding pixels share the same row index. This reduces the correspondences search space to 1D and accelerates pixel-wise matching. In contrast to pinhole cameras, the object-to-image space mapping for satellite sensors is usually described with the rational function model (RFM), also known as rational polynomial coefficients (RPC) model [34, 62, 11, 31, 45, 25]. Since standard epipolar geometry is not valid for this projection model, rectification algorithms like [20, 40, 48] cannot be applied. However, [30] have shown that, locally, correspondences are located on a pair of epipolar curves across the images. This finding enables rectification of complete satellite images by resampling the original images along the epipolar curves [67, 68, 42]. Due to computational efficiency and low memory consumption, many reconstruction pipelines employ some variant of SGM for dense stereo matching. The classical SGM is implemented in [13] and they show state-ofthe-art performance on the ISPRS benchmark [50]. [6] investigate the compensation of overcounting [12] in the context of SGM for satellite imagery and observe improved density but decreased precision. A hierarchical version of SGM is employed by [23], [53] to limit the disparity search range and reduce memory footprint and computation time, while also reducing matching ambiguities. [8] and the top-ranked competitors showed state-of-the-art performance on the IARPA satellite benchmark [3] with off-the-shelf SGM implementations from open source libraries [4] and with NASA's open stereo reconstruction software [58]. Beside vanilla SGM, the latter also implements the More Global Matching [14], using a modified cost aggregation scheme that aims for globally more consistent disparities. In order to avoid costly energy minimisation altogether, [65] construct dense correspondence maps from a sparse set of tie points, via edge aware interpolation.

To obtain a consistent representation of the surface, individual stereo models have to eventually be fused. This is typically realized during DSM generation, by binning 3D points from multiple models into a planimetric 2D grid, followed by various filtering strategies to derive a single elevation value per grid cell – accomplished often by simple median filtering [35, 7, 65]. [15] account for changing surface modes (e.g, vegetation) caused by different acquisition dates. They propose k-median clustering for each grid cell and favour observations from lower clusters. In the spirit of bilateral filtering, [49] apply median filtering on heights of multiple neighbouring grid cells that share the same intensities. [36] cast the fusion of multiple stereo models or elevation maps as a convex energy minimization problem and solve it with a primal-dual algorithm, including an additional planarity prior in the form of a TV-L1 and TGV-L1 penalty.

Some approaches circumvent the somewhat cumbersome pairwise processing and subsequent fusion. Notably, early approaches of dense surface refinement were published in [26, 70]. Rasterized surface elevations and the corresponding

object-space appearance are simultaneously estimated using iterative non-linear least squares. Thereby the surface elevations are refined such that gray or RGB values across multiple views (linked by the elevation values) are consistent. Beside the 2.5D representation, and thus the inability to reconstruct 3D surfaces, those early approaches lack proper occlusion handling or any form of geometric regularization. [7] directly estimate a DSM by assigning photometric similarity costs to a regular 3D cost structure in object space. The final elevation map is derived by semi global optimization. However, the authors find only limited gains compared to the more prevalent late fusion of binocular stereo models. Similarly, [66] estimate an elevation grid and additionally fuse semantic information from a set of satellite images and corresponding semantic segmentation maps. To estimate surface elevations, PatchMatch Belief Propagation [1] is employed to maximize an energy function that encourages consistency of appearance and semantics across several images. Additionally, smoothness of semantics, height values and surface orientations are enforced. [46, 47] propose a probabilistic voxel-based model to jointly reconstruct surface voxels and their corresponding colours. To our knowledge, this is the only published method in the satellite domain which is capable of extracting real 3D geometry. It does, however, not include any explicit surface prior, and [43] found that both urban and rural reconstructions are less accurate than those from pairwise matching and late fusion.

Much less research exists for the satellite domain when compared to the conventional pinhole camera model, presumably because of the limited availability of high-resolution data. We thus review relevant work on mesh refinement in the close range and airborne domains. Typical approaches start by reconstructing depth maps, or point clouds with normals, using Multi View Stereo (MVS), for example [55, 19, 24, 21]. Next, they employ a volumetric approach to bootstrap a topologically correct mesh representation (e.g., [29, 28, 63, 37, 71, 18]). For the latest results we refer the interested reader to one of the active MVS and reconstruction benchmarks [57, 56, 32]. In order to recover fine details and improve precision, the vertex positions of such surface meshes can be further refined [10, 64]. An energy composed of the (multi-view) texture transfer error and a smoothness prior is minimised with gradient descent. [38] accelerate the process by limiting the refinement to regions that feature geometric variances. An alternate minimisation of the reprojection error and mesh denoising is given by [39]. A guideline for the mesh refinement by semantic information is pursued in [2, 51]: semantic consistency across views is enforced and smoothness priors for each class are adapted individually. To the best of our knowledge, all refinement algorithms were formulated for pinhole camera models and cannot be directly applied to satellite data.

3. Methodology

The basic idea of photometric mesh refinement is to position the vertices of a mesh surface, such that texture transferred from an image i to any other image j via the surface should match the original texture of the target image j.

As long as the textures are not in correspondence, they give rise to a gradient, which can be propagated through the sensor model to obtain a gradient per vertex, defining the direction in which it should be displaced to increase the texture similarity. Iterative gradient decent yields a refined mesh with maximal similarity, respectively minimal photometric reprojection error. For clarity, we first review the computation of gradients for the pinhole camera model in section 3.1, before extending it to the RFM in section 3.2. Additionally, section 3.3 discusses implementation details.

3.1. Mesh Refinement with Frame Sensors

As a background for the subsequent adaption to satellite imagery we review the computation of gradients induced by photometric (dis-)similarities under the pinhole model. Let S denote the (infinite) set of admissible 2D surface manifolds in \mathbb{R}^3 . The overall photoconsistency \mathcal{M} is composed of individual terms $\mathcal{M}_{ij}: S \to \mathbb{R}^1$ that measure the photoconsistency between image $\mathcal{I}_j: \Omega_j \to \mathbb{R}^1$ to image $\mathcal{I}_i: \Omega_i \to \mathbb{R}^1$, when projected onto each other via the surface $S \in S$:

$$\mathcal{M}(S) = \sum_{i} \sum_{j \neq i} \mathcal{M}_{ij}(S). \tag{1}$$

Here Ω_j and Ω_i are the image regions in I_j and I_i that see the same surface area Ω on S. Let $\Pi_j, \Pi_i : \mathbb{R}^3 \to \mathbb{R}^2$ be the projections that map object coordinates to image coordinates of \mathcal{I}_j , respectively \mathcal{I}_i , and let $\Pi_{i,S}^{-1}$ and $\Pi_{j,S}^{-1}$ denote the re-projection from the respective image to the surface S. The transfer function relating image coordinates in the two views is given by $\mathcal{I}_j \circ \Pi_j \circ \Pi_{i,S}^{-1}$, such that the pairwise photoconsistency becomes

$$\mathcal{M}_{ij}(S) = \int_{\Omega_i} M(\mathcal{I}_i, \mathcal{I}_j \circ \Pi_j \circ \Pi_{i,S}^{-1}) d\mathbf{x}_i, \tag{2}$$

where M is a measure of photo-consistency. In our case we seek to minimize the negative zero-normalised cross-correlation $M(\mathbf{a}, \mathbf{b}) = -ZNCC(\mathbf{a}, \mathbf{b})$. Using the chain rule, the variation of \mathcal{M}_{ij} with respect to an infinitesimal variation of the surface is given by

$$\frac{\partial \mathcal{M}_{ij}(S + \epsilon \delta S)}{\partial \epsilon} \bigg|_{\epsilon=0} = \int_{\Omega_i} \partial_2 M(\mathbf{x}_i) D \mathcal{I}_j(\mathbf{x}_j) D \Pi_j(\mathbf{X}) \frac{\partial \Pi_{i,S+\epsilon \delta S}^{-1}(\mathbf{x}_i)}{\partial \epsilon} \bigg|_{\epsilon=0} d\mathbf{x}_i ,$$
(3)

where $\partial_2 M(\mathbf{x}_i)$ denotes the derivative of the similarity measure w.r.t. the second argument \mathcal{I}_j . $D\mathcal{I}_j$ is the gradient in image \mathcal{I}_j and $D\Pi_j$ is the derivative of the object-to-image space mapping w.r.t. an object point on the surface. Let \mathbf{d} be the ray from the projection center of view i through pixel coordinate \mathbf{x}_i . The term

$$\frac{\partial \Pi_{i,\mathcal{S}+\epsilon\delta\mathcal{S}}^{-1}(\mathbf{x}_i)}{\partial \epsilon} \bigg|_{\epsilon=0} \tag{4}$$

represents the change along d when moving the surface by δS . This change

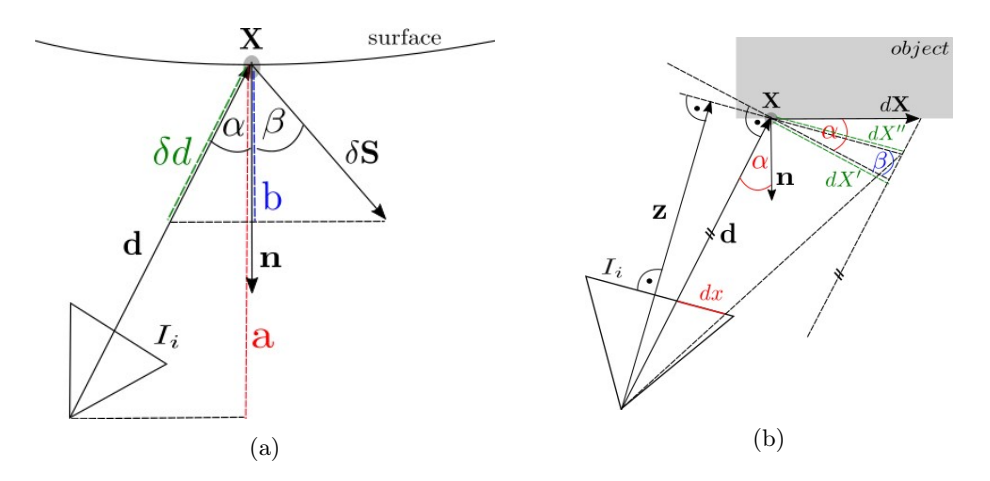


Figure 1: (a): Variation of \mathbf{d} induced by the surface variation $\delta \mathbf{S}$. Let $-\mathbf{n}^T\mathbf{d} = |\mathbf{d}|\cos\alpha := a$ and $\mathbf{n}^T\delta \mathcal{S} = |\delta \mathcal{S}|\cos\beta := b$. The intercept theorem yields $\delta d = |\mathbf{d}|b/a$. (b): Relation of displacement within the surface vs. displacement in the image. From $\cos\alpha = dX'/dX = -\mathbf{n}^T\mathbf{d}/|\mathbf{d}|$ and $\cos\beta = dX'/dX'' = z/|\mathbf{d}|$ follows $dX'' = -dX\mathbf{n}^T\mathbf{d}/z$. The intercept theorem yields $dx = -dX\mathbf{n}^T\mathbf{d}/z^2$

can be computed geometrically using trigonometric functions and the intercept theorem (see figure 1a), which leads to

$$\frac{\partial \Pi_{i,\mathcal{S}+\epsilon\delta\mathcal{S}}^{-1}(\mathbf{x}_i)}{\partial \epsilon} \bigg|_{\epsilon=0} = \frac{\mathbf{n}^T \delta S(\mathbf{X})}{\mathbf{n}^T \mathbf{d}_i} \mathbf{d}_i$$
 (5)

with the surface normal ${\bf n}$. The change in image coordinates caused by an infinitesimal displacement of the object coordinates (see Figure 1b) is computed as

$$d\mathbf{x}_i = -\frac{\mathbf{n}^T \mathbf{d}_i d\mathbf{X}}{z^2}. (6)$$

Here z represents the z-component of a surface point in the camera coordinate system of view i. By substituting (5) in (3), and using (6) to change the integration domain from image space to the surface, we obtain

$$\frac{\partial \mathcal{M}_{ij}(\mathcal{S} + \epsilon \delta \mathcal{S})}{\partial \epsilon} h \bigg|_{\mathbf{c} = 0} = -\int_{\Omega_{\mathcal{S}}} \partial_2 M(\mathbf{x}_i) D \mathcal{I}_j(\mathbf{x}_j) D \Pi_j(\mathbf{X}) \frac{\mathbf{d}_i}{z^2} \mathbf{n}^T \delta \mathcal{S} d\mathbf{X}.$$
 (7)

It has been shown [9, 60] that for the variation $\delta \mathcal{M}$ of the photo-consistency and the variation $\delta \mathcal{S}$ of the surface, the gradient vector field $\nabla \mathcal{M}$ fulfills

$$\delta \mathcal{M} = \frac{\partial \mathcal{M}_{ij}(\mathcal{S} + \epsilon \delta \mathcal{S})}{\partial \epsilon} \bigg|_{\epsilon = 0} = \int_{\Omega_{\mathcal{S}}} \nabla \mathcal{M}_{ij}(S) \delta \mathcal{S} d\mathbf{X}, \tag{8}$$

and the gradient descent flow is given by $-\nabla \mathcal{M}(\mathcal{S})$. Consequently, by comparing (7) and (8), the gradient of the matching function is

$$\nabla \mathcal{M}_{ij}(S) = -\phi_{\Omega_{\mathcal{S}}} \left[\partial_2 M(\mathbf{x}_i) D \mathcal{I}_j(\mathbf{x}_j) D \Pi_j(\mathbf{X}) \frac{\mathbf{d}_i}{z^2} \right] \mathbf{n}. \tag{9}$$

The flag ϕ_{Ω_S} accounts for visibility, evaluating to 1 if the surface is visible in both views $\mathcal{I}_i, \mathcal{I}_j$, and to 0 otherwise. Note that this continuous formulation can be directly used to compute gradients of discrete surfaces, for example triangular meshes. In practice a translation of each single vertex is computed by weighted integration of gradients over its one-ring neighborhood of triangles. For more details the interested reader is referred to [9].

3.2. Mesh Refinement with Spaceborne Pushbroom (Line) Sensors

The de-facto standard to model the object-to-image space mapping for satellite imagery is the RFM. In the following, we derive a mesh refinement scheme like the one above under the RFM (sections 3.2.1-3.2.4). Implementation details for that new model will be given in section 3.3.

3.2.1. Derivatives of the RFM

Since the projection function from object to image space is different from the pinhole model, we first need to adapt the Jacobian $D\Pi(\mathbf{X})$. Let $B_n = B/s_B + o_B$, $L_n = L/s_L + o_L$ and $H_n = H/s_H + o_H$ be normalised geographic lat/lon/height coordinates of an object point, and let $\mathbf{P}(B_n, L_n, H_n)$ be a 20-dimensional vector holding the 3rd-degree polynomial expansion of those normalised coordinates. With the four vectors $\mathbf{N}_s, \mathbf{D}_s, \mathbf{N}_l, \mathbf{D}_l$ each holding 20 rational polynomial coefficients (RPC), the image coordinates of the projected point are

$$\begin{bmatrix} x \\ y \end{bmatrix} = \begin{bmatrix} s_s \frac{\mathbf{N}_s^T \mathbf{P}(B_n, L_n, H_n)}{\mathbf{D}_s^T \mathbf{P}(B_n, L_n, H_n)} + o_l + o_{cl} \\ s_l \frac{\mathbf{N}_s^T \mathbf{P}(B_n, L_n, H_n)}{\mathbf{D}_l^T \mathbf{P}(B_n, L_n, H_n)} + o_s + o_{cs} \end{bmatrix} , \tag{10}$$

with s_s , s_l the scales and offsets between pixels and normalised image coordinates. The RFM parameters shipped with an image tend to only be correct up to a small, global bias. That error is often compensated with an additional affine transformation [17], or with only a translation [16]. We follow the latter and apply only a simple shift correction $[o_{cl}, o_{cs}]$. The 2×3 Jacobian matrix $D\Pi(\mathbf{X})$ w.r.t the geographic coordinates reads

$$D\Pi(B, L, H) = \begin{bmatrix} s_s \frac{\mathbf{N}_s^T \mathbf{P} \mathbf{D}_s^T}{(\mathbf{D}_s^T \mathbf{P})^2} \begin{bmatrix} \frac{1}{s_B} \frac{\partial \mathbf{P}}{\partial B_n} & \frac{1}{s_L} \frac{\partial \mathbf{P}}{\partial L_n} & \frac{1}{s_H} \frac{\partial \mathbf{P}}{\partial H_n} \end{bmatrix} \\ s_l \frac{\mathbf{N}_l^T \mathbf{P} \mathbf{D}_l^T}{(\mathbf{D}_l^T \mathbf{P})^2} \begin{bmatrix} \frac{1}{s_B} \frac{\partial \mathbf{P}}{\partial B_n} & \frac{1}{s_L} \frac{\partial \mathbf{P}}{\partial L_n} & \frac{1}{s_H} \frac{\partial \mathbf{P}}{\partial H_n} \end{bmatrix} \end{bmatrix}.$$
(11)

3.2.2. Quasi-Cartesian Coordinate System

The RFM relates Cartesian image coordinates to polar geographic coordinates. For the mesh refinement, it is not only easier, but also numerically advantageous to operate in local Cartesian coordinates. Hence, we transform geographic coordinates [B, L, H] into a "Quasi-Cartesian" local coordinate system. This can be achieved by scaling latitude B and longitude L to the (metric) unit of the height component H. Let $\mathbf{X}_{geo} = [B_c, L_c, H_c]^T$ be a point located at the center of the area of interest and $\mathbf{X}_{utm} = [X_c, Y_c, H_c]^T$ its UTM coordinates. Furthermore, let $[B_{c+1}, L_{c+1}, H_c]^T$ be the corresponding geographic coordinates of $[X_c + 1.0, Y_c + 1.0, H_c]^T$. Then the transformation to a local, quasi-Cartesian frame can be expressed as

$$\mathbf{X}_{loc} = f(B, L, H) = \left[\frac{B}{B_c - B_{c+1}}, \frac{L}{L_c - L_{c+1}}, H\right]^T - \mathbf{X}_{geo}.$$
 (12)

This transformation mimics a Cartesian coordinate system only locally, but the approximation is valid for a large enough area (refinement of large areas will in practice always be done for local tiles, in order to parallelise the computation). The quality of the approximation (non-orthogonality and scale anisotropy of the coordinate axes) is shown in Table 1. Using the chain rule, the Jacobian of the transformation from image space to quasi-Cartesian coordinates reads

$$D\Pi(X,Y,H) = \begin{bmatrix} \frac{1}{B_c - B_{c+1}} & \frac{1}{L_c - L_{c+1}} & 1\\ \frac{1}{B_c - B_{c+1}} & \frac{1}{L_c - L_{c+1}} & 1 \end{bmatrix} \odot D\Pi(B,L,H), \tag{13}$$

with \odot denoting element-wise multiplication.

3.2.3. Independence of Projection Center and Approximation of Depth

The geometric derivations of (5) and (6) are based on the depth z, and on the ray \mathbf{d} connecting the projection center and a surface point. The RFM does not model a single projection centre. Fortunately, (5) is in fact independent of the absolute length $d = |\mathbf{d}|$. This can be seen by rescaling it to an arbitrary length, e.g., to the unit vector, $\mathbf{d} = d\mathbf{n}_d$. Equation (5) then becomes

$$\frac{\partial \Pi_{i,\mathcal{S}+\epsilon\delta\mathcal{S}}^{-1}(\mathbf{x}_i)}{\partial \epsilon} \bigg|_{\epsilon=0} = \frac{\mathbf{n}^T \delta S(\mathbf{X})}{\mathbf{n}^T \mathbf{n}_d} \mathbf{n}_d. \tag{14}$$

In contrast, for the variation of image space coordinates \mathbf{x}_i ((6)) the length of \mathbf{d} does not cancel out easily. Instead, we use the fact that for large focal lengths $d \approx z$. Thus, the denominator is approximately $\frac{1}{z}$. In other words, a stereo model contributes to the gradient inversely proportional to its distance from the surface. We account for this weighting by scaling with the GSD g at the average terrain height. As $\frac{1}{z} \sim g$, this corresponds to a change of variables

$$d\mathbf{x}_i = -g\mathbf{n}^T \mathbf{n}_{d,i} d\mathbf{X},\tag{15}$$

and the final gradient is calculated as

$$\nabla \mathcal{M}_{ij}(S) = -\phi_{\Omega_S} \left[\partial_2 M(\mathbf{x}_i) D \mathcal{I}_i(\mathbf{x}_i) D \Pi_i(\mathbf{X}) g \mathbf{n}_{d,i} \right] \mathbf{n}. \tag{16}$$

3.2.4. Approximation of Straight Rays With Virtual Cameras

Computing the derivative of the similarity measure $\partial_2 M$ requires mapping the image \mathcal{I}_j into the view i via the surface, which involves ray casting. Viewing rays modeled by the RFM are in general not straight lines which prevents efficient ray casting. In practice one can assume that the curvature of the rays is low enough to represent them by straight rays in the vicinity of the surface (see Table 2). Therefore, we define a virtual camera in the following way: We define two virtual planes in object space with constant heights h and $h + \Delta h$ above ground. Then each image pixel is projected to those two planes using the RFM (and mapped to quasi-Cartesian coordinates), to obtain two virtual points $\mathbf{v} = [x, y, h]$ and $\mathbf{v}' = [x', y', h + \Delta h]$. The set of line segments $(\mathbf{v}' - \mathbf{v})$, together with the corresponding pixel intensities, forms a virtual camera that observes the surface along straight rays.

3.3. Implementation Details

The overall pipeline for surface refinement proceeds as follows: First, the input mesh is transformed to quasi-Cartesian coordinates. Next, two virtual cameras \mathcal{I}_i^v , \mathcal{I}_i^v are set up for each stereo pair. Now the iterative refinement starts; the image intensities of \mathcal{I}_i^v are projected onto the current surface and back into \mathcal{I}_i . There, we densely compute the similarity (in our implementation ZNCC) between the original and the projected images, as well as its derivative. From \mathcal{I}_i^v we read out the ray direction \mathbf{n}_d . The remaining components needed to compute the gradient (16) are obtained as discussed in sections 3.2.1-3.2.4. Per-vertex gradients are obtained by integrating (16) over all faces in a one-ring neighborhood. For each vertex of the input mesh, the resulting gradients are summed over all stereo models and scaled with the step size to obtain a field of vertex displacements. To these photometric gradients, we add displacement vectors corresponding to the thin-plate energy [33] to regularise the surface smoothness [64]. The final displacement field is applied to the mesh vertices to obtain an updated surface, which then serves as input to the next iteration. Formally, the overall energy is given as

$$E(\mathcal{S}) = \alpha \mathcal{M}(\mathcal{S}) + \beta \int_{\mathcal{S}} (\kappa_1 + \kappa_2) d\mathcal{S}, \tag{17}$$

where $\kappa 1$, $\kappa 2$ denote the principal curvatures of the surface. The weight α balances the photometric term and the smoothness. Homogenisation of smoothness and photometric energies is achieved with an additional parameter $\beta = \frac{1}{gsd^2}$ that account for different scales across datasets and mesh resolutions.

In all experiments we run 20 iterations of gradient descent, after which the energy barely decreases any more. More advanced stopping criteria are of course possible. The weight factor α and the step size for gradient decent were derived by grid search.

We observed convergence problems for input meshes with vertices located too far from the correct surface. We found that convergence can be improved by a hierarchical processing scheme, similar to [38]. To that end, we convert

the input mesh to a cloud of oriented points and extract a low-resolution mesh via Poisson reconstruction [29]. Thereby we choose the minimal voxel resolution (respectively, octree leaf dimension) to 2^l GSD. The low-resolution mesh is refined using downscaled versions of the original images (factor 2^l) for 20 iterations. Then the mesh is densified by splitting each triangle face into four smaller ones, and refinement is repeated with image scale 2^{l-1} , and so forth until the full resolution is reached. Note that the densification factor is the same as the increase in the number of pixels from one pyramid level to the next, hence the (average) number of pixels per triangle remains the same. In our current implementation a triangle covers 2 pixels in average. For additional implementation details we refer the interested reader to our publicly accessible implementation of mesh refinement for pinhole models published in [2].

scale s	length $ \mathbf{x}' _2$ [m]	length $ \mathbf{y}' _2$ m	angle \mathbf{x}', \mathbf{y}' [deg]
100	100.002	100.002	90.000
200	200.003	200.003	90.001
500	500.009	500.008	90.001
1000	1000.018	1000.016	90.003
2000	2000.038	2000.031	90.005
5000	5000.110	5000.067	90.014

Table 1: Approximation error of the quasi-Cartesian local coordinate system. To check orthogonality we define two orthogonal unit vectors $\mathbf{x} = \mathbf{p}_1 - \mathbf{p}_0$ and $\mathbf{y} = \mathbf{p}_2 - \mathbf{p}_0$ in UTM coordinates. \mathbf{p}_0 is located in the center of the test area described in section 4.1. The points $\mathbf{p}_{0,1,2}$ are located in a horizontal plane at the average terrain height. We transform scaled versions $s\mathbf{x}$ ad $s\mathbf{y}$ to geographic coordinates and then to the quasi-Cartesian frame to obtain \mathbf{x}' and \mathbf{y}' . For vectors of length 2000m the scale difference in x- and y-direction is <7mm, the deviation of x- and z-axis is 38mm, or 0.13 times the GSD of the best available civilian satellite imagery, which is well below the absolute precision of the RPC projection. The angle between \mathbf{x}' and \mathbf{y}' is <0.006°

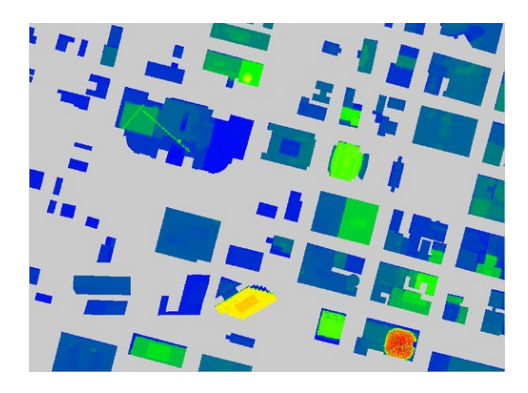
	hr	n	1	100	500	1000
ĺ	ϕ	0	30.131	30.130	30.128	30.126

Table 2: Approximation of off-nadir ray angles ϕ . The table displays the direction of a ray close to the surface, approximated with our virtual camera construction. By varying h it can be seen that the rays are indeed slightly curved. However, the difference between h=0m and h=1000m is ≈ 0.005 °. In other words, the error of the virtual camera approximation is negligible for any reasonable camera height h.

4. Results

4.1. Test Sites

We test the proposed algorithm on the publicly available benchmark [5], which provides multi-view collections of 16bit panchromatic WorldView-3 images with 0.3m GSD (at nadir, the actual GSD in off-nadir views can be up to a factor of ≈ 1.5 lower). Two different test sites were evaluated: Downtown Jacksonville (JAX), FL, USA and University of California San Diego (UCSD), CA,



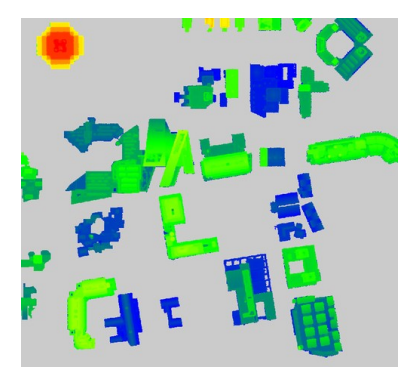


Figure 2: Ground truth LiDAR DSM data of evaluated building areas of JAX test site (left) and UCSD test site (right).

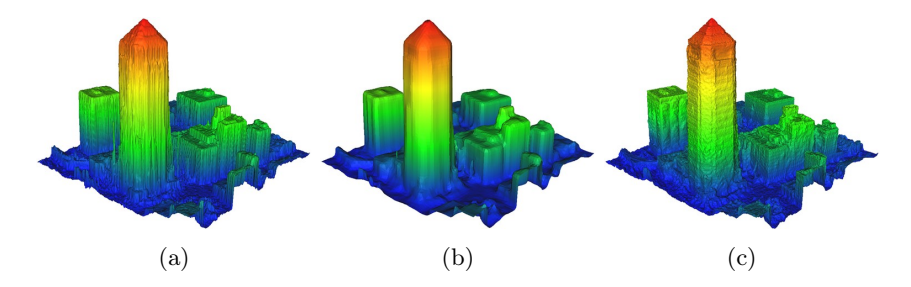


Figure 3: Example of (a) the DSM mesh (b) the input Poisson mesh (c) the refined mesh for region of interest (JAX).

USA. The JAX test site features 26 images of an urban area of ca. 750m×750m, collected between October 2014 and February 2016. The UCSD test site consists of 35 images covering an area of ca. 600m×600m, collected between October 2015 and August 2017. A 2.5D LiDAR DSM with 0.5m GSD is provided and serves as ground truth for both test sites, see Figure 2. The lack of full-3D ground truth makes it impossible to quantitatively evaluate 3D elements, such as indentations on facades, in our reconstructed mesh, see Figure 3(c). Nevertheless, since the gist of our approach is its ability to reconstruct true 3D geometry, we first present a qualitative evaluation of such 3D areas in the following section, while the quantitative evaluation based on 2.5D elevation maps is discussed in section 4.4.

4.2. Generation of Initial Meshes, Pre-Processing and Parameters

The proposed mesh refinement needs an initial surface mesh to start from. We generate that mesh by running conventional dense stereo and meshing the resulting 2.5D elevation model by Poisson reconstruction (Section 3.3). The MVS system requires sub-pixel accurate relative alignment for good performance, which is not reached by the image provider's RPCs. We use RFM

parameters that have been refined with the method of [44], which implements bias-correction via feature matching and subsequent bundle block adjustment.

The image collections feature very high redundancy, almost all images of a site have significant overlap. It would not be meaningful to use possible pairings for surface reconstruction: not only would it be computationally expensive, it can also be harmful to include images with baselines too short for accurate triangulation or too long for robust matching. According to our experimental experience and related research [7, 15, 49], we manually remove images with overly poor illumination conditions and select 80 suitable image pairs for JAX and 86 for UCSD, with intersection angles of the viewing directions between 5° and 13°. The parameter α which controls the contribution of the unary term was set to $3.5 \cdot 10^4$ for UCSD and $4 \cdot 10^4$ for JAX respectively. The parameter β , which steers the smoothness was set to 0.05 for both datasets. The average size of projected triangles is 2 pixels. Meshes were refined using the coarse-to-fine scheme starting at 1/8 resolution and stopping at the full resolution images. With the current, unoptimised implementation the runtime for the full-resolution refinement is 65mins for JAX and 39mins for the samller UCSD. The most time consuming part is ray casting, which consumes $\approx 70\%$ of the computation time. We note that the ray casting is suitable for GPU implementation, as is the computation of $\partial M(\mathbf{x}_i)$, which furthermore could be reused and updated only periodically after several iterations. Together with stricter mechanisms for stereo-pair selection and masking of regions outside the stereo overlap, a $>10\times$ speed-up is almost certainly possible.

4.3. Qualitative Evaluation - Reconstruction of 3D Structure

In this section we qualitatively assess the reconstructions obtained with the proposed 3D mesh refinement algorithm. In particular, we illustrate its ability to recover 3D shape details that are not representable in a 2.5D height field, and its superior treatment of sharp discontinuities on man-made structures. Figure 4 shows 2.5D tSGM models (4a, 4d, 4g, 4j), the refined 3D models (4b, 4e, 4h, 4k) and Google Maps snapshots (4c, 4f, 4i, 4l) of four example regions of interest (ROIs). Facades of the building displayed in figure 4e are clearly smoother than in the 2.5D version displayed in 4d. For 2.5D models, the facade geometry is defined by roof and ground elevations. Errors in such elevation estimates are propagated over the whole facade. 3D refinement in facade regions is supported by image similarity in oblique views, leading to smoother surfaces without raster artifacts, and without destroying high-frequency crease edges. Thus, the refined models have visibly crisper crease edges. On the building in the first row, there are improvements of the roof geometry (little steps). Such shapes are inherently difficult for 2.5D approaches, where these elements are represented only by very few pixels of the elevation map. Moreover, the facades feature indentations and vertical edges that are, by construction, not representable in a 2.5D heightfield. Similar observations hold for the buildings in the second and third rows: Roof substructures are crisper and more geometric detail is extracted on facades. However, the facades are overly bumpy in places, presumably due to repetitive structures, specular materials and insufficient evidence in the image set due to the uneven distribution of viewing directions. For the challenging case in the fourth row vertical roof structures are only partly reconstructed, apparently due to weak data support. Also the large, dark glass surfaces again impair the facade reconstruction.

Figures 5a-5f depict surfaces of vegetation, bridges, thin roof structures and railway tracks. Compared to tSGM, refined surfaces offer more detail, feature less outliers and appear less noisy. The same holds true for reconstructed vegetation. The street under the bridge (Figure 5e) is not reconstructed correctly – while one can see the attempt to "carve out" the empty space under the bridge, the refinement is limited by the faulty topology of the initial surface, which cannot be changed by the algorithm.

4.4. Quantitative Evaluation of Multi-View Refinement

To test the sensitivity of our method w.r.t. the initialisation, we generate DEMs with three different state-of-the-art satellite MVS systems: (a) [23] using a hierarchical version of SGM [53], (b) the S2P pipeline [15] based on MGM [14], and (c) NASA's Stereo Pipeline (ASP) [41] based on Semi-Global-Block-Matching [4]. The three DEMs also serve as baselines to compare with. For a fair comparison we use the refined RFM parameters in all MVS systems and in the actual mesh refinement.

The LiDAR ground truth is provided in the form of a 2.5D gridded DEM. Consequently, the refined 3D meshes must be converted back to 2.5D elevation maps. To accomplish this process, we align the mesh to the LiDAR DEM [3], cast a vertical ray through the centre of each grid cell, and extract the highest intersection point with the reconstructed mesh.

4.4.1. Evaluation of Refined Surfaces in Benchmark Regions

Table 3 displays error statistics for the MVS results and the corresponding refinement results, for both test sites. The comparisons to ground truth were carried out with the test suite provided by [3], where we add additional, robust error metrics: namely, a truncated root mean square error RMSE, computed from only those residuals that are <3m (ca. 10GSD), and the corresponding completeness (percentage of residuals below that threshold). Furthermore, we list the normalised median absolute residuals and the 68% percentile of absolute residuals, denoted by perc-68. This value is calculated such, that 68% of the residuals are \leq perc-68, corresponding to $\pm 1 \cdot \sigma$ of a Gaussian error distribution. Note that the framework evaluates only on selected building roofs, see Figure 2, to rule out error sources like seasonal changes, extreme height discontinuities, temporal changes and moving objects. [5] provide a building mask for the Jacksonville test site. Since for the UCSD site the building mask is not publicly available, we manually created one. As shown in table 3, our mesh refinement significantly improves the 2.5D DEMs generated with both the SGM and ASP methods. There are no significant quantitative differences to S2P (for JAX the refined version is insignificantly better, for UCSD insignificantly worse). We note that the error metrics do not fully reflect the visual quality of the reconstructions. The mesh refinement does bring out additional 3D structure and

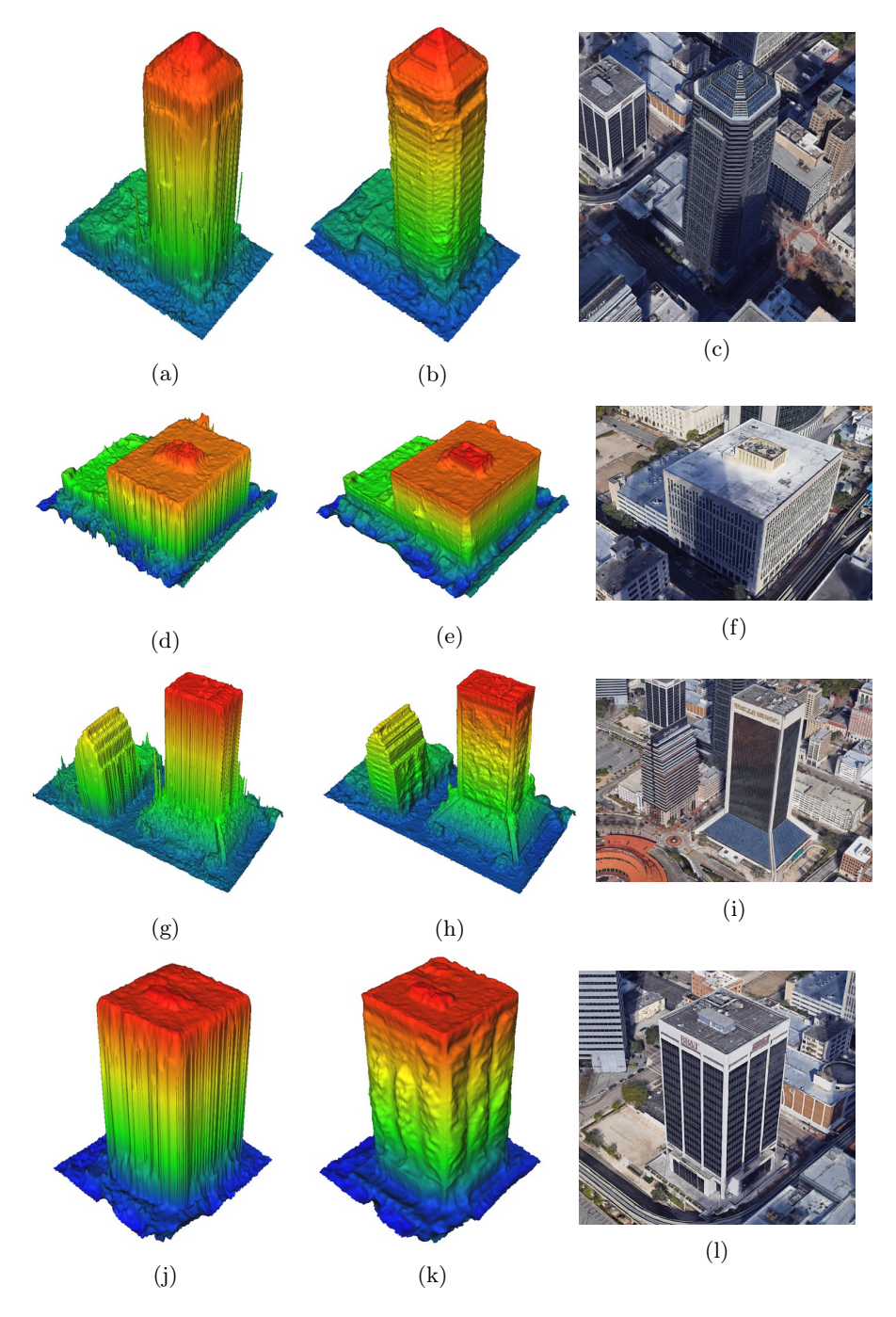


Figure 4: Visualization of building surfaces generated by tSGM (left column), the refined versions (middle column) and Google Maps snapshots (right column).

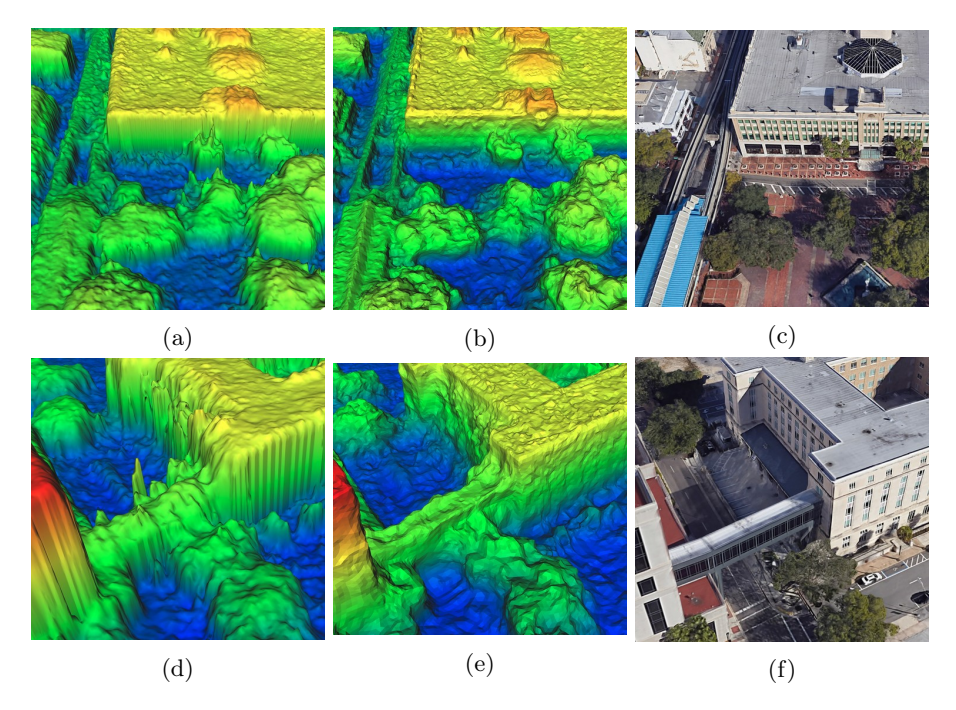


Figure 5: Visualization of general surfaces generated by tSGM (left column), the refined versions (middle column) and Google Maps snapshots (right column).

suppress noise (see Sec. 4.4.2), but it appears that in terms of average 2.5D roof accuracy the S2P method is already close to the achievable limit (normalised median absolute deviation $<1.5\,\mathrm{GSD}$), so that no further improvement is possible. In general, the accuracy of the DEMs, at least on roof surfaces, is in the sub-metre range, which we find very encouraging. The majority of the residuals are $<1.5\,\mathrm{GSD}$. Note that the mesh refinement exhibits little sensitivity to the initialisation, its results are quantitatively very similar in all cases, independent of which stereo method was used to generate the input surface.

4.4.2. In-depth Evaluation of Refined Surfaces on Individual Buildings

To characterise the reconstruction in more detail and gain further insights into its behaviour, we examine four building roofs for each test site in detail. As explained in section 4.4.1 we exclude building edges, since aliasing at large height jumps makes a meaningful evaluation impossible.

Figures 6 and 7 display exemplary surface reconstructions of the different tested methods for both ROIs. Tables 4 and 5 list the corresponding quantitative results. Again, mesh refinement generally improves the accuracy over SGM and ASP, at both sites. With S2P we get mixed results. Its accuracy is already very high (for several buildings at, or below GSD), so the results after refinement are quantitatively almost the same. Still, visual inspection makes clear that the quantitative metrics do not fully characterise the model quality: The

		tSGM	tSGM ref	S2P	SP2 ref	ASP	ASP ref
Ĺ.,	Compl. [%]	88.46	88.77	88.32	88.39	84.22	87.14
X	RMSE [m]	0.86	0.80	0.79	0.78	1.0	0.83
JA	NMAD [m]	0.51	0.39	0.42	0.40	0.74	0.46
	perc-68 [m]	0.88	0.73	0.72	0.71	1.25	0.80
	Compl. [%]	95.69	96.09	96.78	96.12	93.23	96.44
JCSD	RMSE [m]	0.97	0.86	0.82	0.85	1.16	0.86
	NMAD [m]	0.58	0.47	0.45	0.46	0.79	0.47
-	perc-68 [m]	0.95	0.77	0.74	0.75	1.28	0.77

Table 3: Evaluation results of the JAX and UCSD test site for three MVS methods ([23, 15, 41]) and corresponding refined surfaces (marked by 'ref').

		tSGM	tSGM ref	S2P	SP2 ref	ASP	ASP ref
1	Compl. [%]	92.69	93.35	93.82	92.83	89.76	90.57
	RMSE [m]	0.80	0.79	0.67	0.77	0.85	0.76
ROI	NMAD [m]	0.31	0.24	0.22	0.23	0.46	0.25
	perc-68 [m]	0.70	0.64	0.51	0.56	0.85	0.61
7	Compl. %	94.69	94.71	95.06	94.54	89.71	93.49
	RMSE [m]	0.77	0.75	0.69	0.74	1.07	0.75
ROI	NMAD [m]	0.37	0.28	0.27	0.30	0.67	0.30
"	perc-68 [m]	0.71	0.64	0.60	0.62	1.22	0.65
ಣ	Compl. [%]	79.31	80.54	83.79	80.86	63.26	80.37
	RMSE [m]	1.26	1.18	1.15	1.13	1.56	1.16
ROI	NMAD [m]	1.18	1.00	0.88	0.87	2.15	0.92
"	quant-68 [m]	1.93	1.75	1.52	1.68	3.32	1.78
4	Compl. [%]	93.68	$\boldsymbol{95.52}$	94.63	94.86	88.81	92.64
1	RMSE[m]	0.89	0.76	0.82	0.74	1.05	0.75
ROI	NMAD [m]	0.46	0.36	0.36	0.35	0.67	0.36
"	perc-68 [m]	0.84	0.66	0.68	0.63	1.20	0.68

Table 4: Evaluation results of the JAX test site for three MVS methods ([23, 15, 41]) and corresponding refined surfaces (marked by 'ref').

		tSGM	tSGM ref	S2P	SP2 ref	ASP	ASP ref
1	Compl. [%]	99.70	99.20	98.50	99.0	94.40	99.04
	RMSE [m]	0.97	0.87	0.86	0.88	1.21	0.86
RO	NMAD [m]	0.61	0.50	0.48	0.52	0.90	0.51
"	perc-68 m	0.90	0.74	0.74	0.75	1.34	0.73
2	Compl. %	92.46	92.22	94.17	92.33	86.15	91.80
	RMSE [m]	1.12	0.97	0.96	0.97	1.24	0.98
RO	NMAD [m]	0.68	0.52	0.48	0.52	0.90	0.54
"	perc-68 m	1.22	0.93	0.92	0.92	1.67	0.96
ಣ	Compl. [%]	96.00	98.67	97.66	98.33	85.21	98.31
=	RMSE [m]	1.10	1.07	1.09	1.10	1.65	1.12
RO	NMAD [m]	0.69	0.59	0.67	0.61	1.60	0.69
"	perc-68 m	1.09	1.06	1.10	1.10	2.27	1.17
4	Compl. %	99.14	99.44	99.53	99.52	96.44	99.31
	RMSE [m]	0.95	0.95	0.88	0.94	1.35	0.96
RO	NMAD [m]	0.57	0.46	0.46	0.45	0.70	0.43
	perc-68 m	0.92	0.85	0.83	0.84	1.48	0.87

Table 5: Evaluation results of the UCSD test site for three MVS methods ([23, 15, 41]) and corresponding refined surfaces (marked by 'ref').

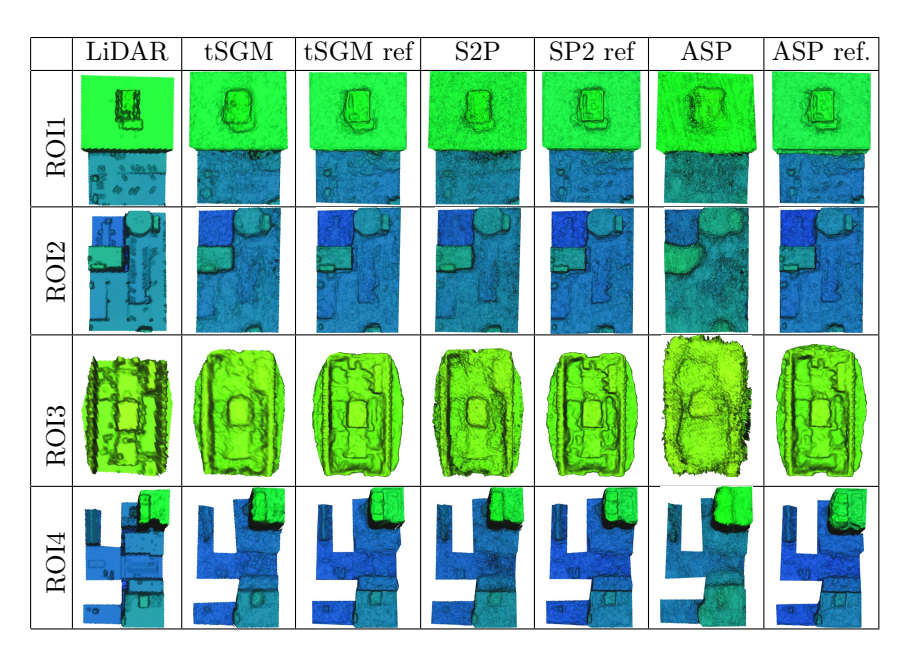


Table 6: Visualization of the building evaluation for the JAX test site from table 4.

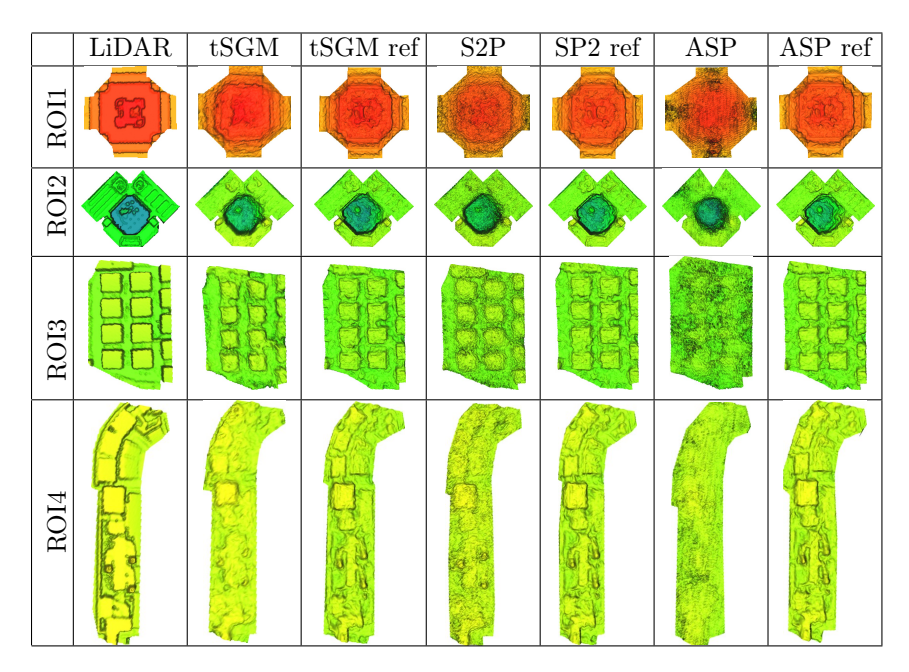


Table 7: Visualization of the building evaluation for the UCSD test site from table 5.

refined surfaces are crisper and more correct on complicated roof structures. The numbers do not reflect this, because after refinement the surface tends to be slightly noisier on flat, fronto-parallel areas that play to the strength of the constant-height prior built into most MVS and 2.5D fusion methods. Overall, we observe crisper reconstructions of roof details after refinement. These details are recovered even when starting from the roughest initial surface (generated with NASA's ASP), where they are completely missing. The meshes after refinement are also visually comparable, independent of the initialisation, indicating favourable convergence properties of the hierarchical optimisation. We note in passing that the 68-percentile metric is comparable with the numbers published in [5].

5. Conclusion

We have presented an algorithm to refine 3D surface meshes by minimising the photometric transfer error between multiple pairs of satellite images, whose sensor poses are specified through the RFM.

In experiments on high-resolution data from WorldView-3, we have shown that, compared to the input from state-of-the-art MVS pipelines, the refinement extracts additional 3D surface details and better reproduces crisp edges and discontinuities. It also decreases the residual errors of the recovered surface in most cases. Being based on image similarity, it is however still challenged by repetitive texture and non-Lambertian surfaces. To further diminish artefacts of our method in such areas, one important direction is to endow 3D surface models with more a-priori knowledge about the reconstructed scene. In particular, our current implementation includes only a simple thin-plate regulariser to favour low curvature. Elementary priors like the preference for piecewise constant heights (extensively used in dense matching and 2.5D model fusion), or a preference for right angles, are still missing and need to be ported to the world of 3D mesh-based reconstruction.

A major difference to existing reconstruction pipelines is that our algorithm is able to handle true 3D geometry. We have shown that, when including oblique satellite views, the method produces cleaner facade structures and recovers facade details. This property could be advantageous for downstream building modelling, surface structuring and analysis based on geometric features, and of course visual display from off-nadir viewpoints. We believe that with the growing availability of high-resolution, oblique satellite images the field could move beyond 2.5D elevation models and the quest for full 3D models will gain momentum. We hope that our work triggers further research in that direction.

References

References

- [1] Besse, F.O., 2013. PatchMatch Belief Propagation for Correspondence Field Estimation and its Applications. Ph.D. thesis. University College London (UCL).
- [2] Blaha, M., Rothermel, M., Oswald, M.R., Sattler, T., Richard, A., Wegner, J.D., Pollefeys, M., Schindler, K., 2017. Semantically informed multiview surface refinement, in: Proceedings of the IEEE International Conference on Computer Vision, pp. 3819–3827.
- [3] Bosch, M., Kurtz, Z., Hagstrom, S., Brown, M., 2016. A multiple view stereo benchmark for satellite imagery, in: Proceedings of the IEEE Applied Imagery Pattern Recognition Workshop (AIPR), pp. 1–9.
- [4] Bradski, G., 2000. The OpenCV Library. Dr. Dobb's Journal of Software Tools .
- [5] Brown, M., Goldberg, H., Foster, K., Leichtman, A., Wang, S., Hagstrom, S., Bosch, M., Almes, S., 2018. Large-scale public lidar and satellite image data set for urban semantic labeling, in: Proceedings of Laser Radar Technology and Applications XXIII, pp. 154–167.
- [6] d'Angelo, P., 2016. Improving semi-global matching: Cost aggregation and confidence measure. International Archives of the Photogrammetry, Remote Sensing and Spatial Information Sciences 41, 299–304.
- [7] d'Angelo, P., Kuschk, G., 2012. Dense multi-view stereo from satellite imagery, in: Proceedings of 2012 IEEE International Geoscience and Remote Sensing Symposium, pp. 6944–6947.
- [8] De Franchis, C., Meinhardt-Llopis, E., Michel, J., Morel, J.M., Facciolo, G., 2014. An automatic and modular stereo pipeline for pushbroom images. ISPRS Annals of the Photogrammetry, Remote Sensing and Spatial Information Sciences 2, 49–56.
- [9] Delaunoy, A., Prados, E., 2011. Gradient flows for optimizing triangular mesh-based surfaces: Applications to 3d reconstruction problems dealing with visibility. International journal of computer vision 95, 100–123.
- [10] Delaunoy, A., Prados, E., Piracés, P.G.I., Pons, J.P., Sturm, P., 2008. Minimizing the multi-view stereo reprojection error for triangular surface meshes, in: Proceedings of BMVC 2008-British Machine Vision Conference, pp. 1–10.
- [11] Dial, G., Grodecki, J., 2002. Block adjustment with rational polynomial camera models, in: Proceedings of ASPRS 2002 Conference, Washington, DC, pp. 22–26.

- [12] Drory, A., Haubold, C., Avidan, S., Hamprecht, F.A., 2014. Semi-global matching: a principled derivation in terms of message passing, in: Proceedings of German Conference on Pattern Recognition, pp. 43–53.
- [13] d'Angelo, P., Reinartz, P., 2011. Semiglobal matching results on the isprs stereo matching benchmark. International Archives of the Photogrammetry, Remote Sensing and Spatial Information Sciences 38, 79–84.
- [14] Facciolo, G., De Franchis, C., Meinhardt, E., 2015. Mgm: A significantly more global matching for stereovision, in: Proceedings of BMVC 2015-British Machine Vision Conference, pp. 1–12.
- [15] Facciolo, G., De Franchis, C., Meinhardt-Llopis, E., 2017. Automatic 3d reconstruction from multi-date satellite images, in: Proceedings of IEEE Conference on Computer Vision and Pattern Recognition, pp. 57–66.
- [16] Fraser, C., Dial, G., Grodecki, J., 2006. Sensor orientation via RPCs. ISPRS Journal of Photogrammetry and Remote Sensing 60, 182–194.
- [17] Fraser, C., Yamakawa, T., 2004. Insights into the affine model for highresolution satellite sensor orientation. ISPRS Journal of Photogrammetry and Remote Sensing 58, 275–288.
- [18] Fuhrmann, S., Gösele, M., 2014. Floating scale surface reconstruction. ACM Transactions on Graphics (ToG) 33, 46:1–46:11.
- [19] Furukawa, Y., Ponce, J., 2010. Accurate, dense, and robust multi-view stereopsis. IEEE Transactions on Pattern Analysis and Machine Intelligence 32, 1362–1376.
- [20] Fusiello, A., Trucco, E., Verri, A., 2000. A compact algorithm for rectification of stereo pairs. Machine Vision and Applications 12, 16–22.
- [21] Galliani, S., Lasinger, K., Schindler, K., 2016. Gipuma: Massively parallel multi-view stereo reconstruction. Publikationen der Deutschen Gesellschaft für Photogrammetrie, Fernerkundung und Geoinformation e. V 25, 361– 369.
- [22] Gehrig, S.K., Franke, U., 2007. Improving stereo sub-pixel accuracy for long range stereo, in: Proceedings of 2007 IEEE 11th International Conference on Computer Vision, pp. 1–7.
- [23] Gong, K., Fritsch, D., 2019. DSM generation from high resolution multiview stereo satellite imagery. Photogrammetric Engineering & Remote Sensing 85, 379–387.
- [24] Gösele, M., Snavely, N., Curless, B., Hoppe, H., Seitz, S.M., 2007. Multiview stereo for community photo collections, in: Proceedings of 2007 IEEE 11th International Conference on Computer Vision, pp. 1–8.

- [25] Hartley, R.I., Saxena, T., 1997. The cubic rational polynomial camera model, in: Proceedings of the DARPA Image Understanding Workshop, pp. 649–653.
- [26] Helava, U., 1988. Object-space least-squares correlation, in: (ACSM and American Society for Photogrammety and Remote Sensing, Annual Convention, Saint Louis, MO, Mar. 14-18, 1988) Photogrammetric Engineering and Remote Sensing, pp. 711-714.
- [27] Hirschmüller, H., 2008. Stereo processing by semiglobal matching and mutual information. IEEE Transactions on pattern analysis and machine intelligence 30, 328–341.
- [28] Jancosek, M., Pajdla, T., 2011. Multi-view reconstruction preserving weakly-supported surfaces, in: Proceedings of IEEE Conference on Computer Vision and Pattern Recognition, pp. 3121–3128.
- [29] Kazhdan, M., Hoppe, H., 2013. Screened poisson surface reconstruction. ACM Transactions on Graphics (ToG) 32, 29:1–29:13.
- [30] Kim, T., 2000. A study on the epipolarity of linear pushbroom images. Photogrammetric Engineering & Remote Sensing 62, 961–966.
- [31] Kim, T., Dowman, I., 2006. Comparison of two physical sensor models for satellite images: position–rotation model and orbit–attitude model. The Photogrammetric Record 21, 110–123.
- [32] Knapitsch, A., Park, J., Zhou, Q.Y., Koltun, V., 2017. Tanks and temples: Benchmarking large-scale scene reconstruction. ACM Transactions on Graphics 36, 78:1–78:13.
- [33] Kobbelt, L., Campagna, S., Vorsatz, J., Seidel, H.P., 1998. Interactive multi-resolution modeling on arbitrary meshes, in: Proceedings of the 25th Annual Conference on Computer Graphics and Interactive Techniques, pp. 105–114.
- [34] Kratky, V., 1989. On-line aspects of stereophotogrammetric processing of spot images. Photogrammetric Engineering and Remote Sensing 55, 311– 316.
- [35] Kuschk, G., 2013. Large scale urban reconstruction from remote sensing imagery. International Archives of the Photogrammetry, Remote Sensing and Spatial Information Sciences 40, 139–146.
- [36] Kuschk, G., d'Angelo, P., Gaudrie, D., Reinartz, P., Cremers, D., 2017. Spatially regularized fusion of multiresolution digital surface models. IEEE Transactions on Geoscience and Remote Sensing 55, 1477–1488.
- [37] Labatut, P., Pons, J.P., Keriven, R., 2009. Robust and efficient surface reconstruction from range data. Computer graphics forum 28, 2275–2290.

- [38] Li, S., Siu, S.Y., Fang, T., Quan, L., 2016. Efficient multi-view surface refinement with adaptive resolution control, in: Proceedings of European Conference on Computer Vision, pp. 349–364.
- [39] Li, Z., Wang, K., Zuo, W., Meng, D., Zhang, L., 2015. Detail-preserving and content-aware variational multi-view stereo reconstruction. IEEE Transactions on Image Processing 25, 864–877.
- [40] Loop, C., Zhang, Z., 1999. Computing rectifying homographies for stereo vision, in: Proceedings of IEEE Conference on Computer Vision and Pattern Recognition, pp. 125–131.
- [41] Moratto, Z.M., Broxton, M.J., Beyer, R.A., Lundy, M., Husmann, K., 2010. Ames stereo pipeline, nasa's open source automated stereogrammetry software, in: Proceedings of Lunar and Planetary Science Conference, p. 2364.
- [42] Oh, J., 2011. Novel Approach to Epipolar Resampling of HRSI and Satellite Stereo Imagery-based Georeferencing of Aerial Images. Ph.D. thesis. The Ohio State University.
- [43] Ozcanli, O.C., Dong, Y., Mundy, J.L., Webb, H., Hammoud, R., Tom, V., 2015. A comparison of stereo and multiview 3-d reconstruction using crosssensor satellite imagery, in: Proceedings of IEEE Conference on Computer Vision and Pattern Recognition, pp. 17–25.
- [44] Patil, S., Comandur, B., Prakash, T., Kak, A.C., 2019. A new stereo benchmarking dataset for satellite images. Computing Research Repository abs/1907.04404. URL: http://arxiv.org/abs/1907.04404.
- [45] Poli, D., Toutin, T., 2012. Review of developments in geometric modelling for high resolution satellite pushbroom sensors. The Photogrammetric Record 27, 58–73.
- [46] Pollard, T., Mundy, J.L., 2007. Change detection in a 3-d world, in: Proceedings of IEEE Conference on Computer Vision and Pattern Recognition, pp. 1–6.
- [47] Pollard, T.B., Eden, I., Mundy, J.L., Cooper, D.B., 2010. A volumetric approach to change detection in satellite images. Photogrammetric Engineering & Remote Sensing 76, 817–831.
- [48] Pollefeys, M., Koch, R., Van Gool, L., 1999. A simple and efficient rectification method for general motion, in: Proceedings of the IEEE International Conference on Computer Vision, pp. 496–501.
- [49] Qin, R., 2017. Automated 3d recovery from very high resolution multi-view satellite images. Computing Research Repository abs/1905.07475. URL: https://arxiv.org/abs/1905.07475.

- [50] Reinartz, P., d'Angelo, P., Krauß, T., Poli, D., Jacobsen, K., Buyuksalih, G., 2010. Benchmarking and quality analysis of dem generated from high and very high resolution optical stereo satellite data, in: Proceedings of The 2010 Canadian Geomatics Conference and Symposium of Commission I, ISPRS Convergence in Geomatics Shaping Canada's Competitive Landscape, pp. 1–6.
- [51] Romanoni, A., Ciccone, M., Visin, F., Matteucci, M., 2017. Multi-view stereo with single-view semantic mesh refinement, in: Proceedings of the IEEE International Conference on Computer Vision, pp. 706–715.
- [52] Roth, L., Mayer, H., 2019. Reduction of the fronto-parallel bias for wide-baseline semi-global matching. ISPRS Annals of Photogrammetry, Remote Sensing and Spatial Information Sciences 4, 69–76.
- [53] Rothermel, M., Wenzel, K., Fritsch, D., Haala, N., 2012. SURE: Photogrammetric surface reconstruction from imagery, in: Proceedings of Low-Cost 3D Workshop Berlin, pp. 1–9.
- [54] Scharstein, D., Taniai, T., Sinha, S.N., 2017. Semi-global stereo matching with surface orientation priors, in: Proceedings of International Conference on 3D Vision (3DV), pp. 215–224.
- [55] Schönberger, J.L., Zheng, E., Pollefeys, M., Frahm, J.M., 2016. Pixel-wise view selection for unstructured multi-view stereo, in: Proceedings of European Conference on Computer Vision, pp. 501–518.
- [56] Schöps, T., Schönberger, J.L., Galliani, S., Sattler, T., Schindler, K., Pollefeys, M., Geiger, A., 2017. A multi-view stereo benchmark with high-resolution images and multi-camera videos, in: Proceedings of IEEE conference on Computer Vision and Pattern Recognition, pp. 3260–3269.
- [57] Seitz, S.M., Curless, B., Diebel, J., Scharstein, D., Szeliski, R., 2006. A comparison and evaluation of multi-view stereo reconstruction algorithms, in: Proceedings of IEEE Conference on Computer Vision and Pattern Recognition, pp. 519–528.
- [58] Shean, D.E., Alexandrov, O., Moratto, Z.M., Smith, B.E., Joughin, I.R., Porter, C., Morin, P., 2016. An automated, open-source pipeline for mass production of digital elevation models (dems) from very-high-resolution commercial stereo satellite imagery. ISPRS Journal of Photogrammetry and Remote Sensing 116, 101–117.
- [59] Shimizu, M., Okutomi, M., 2002. Precise subpixel estimation on area-based matching. Systems and Computers in Japan 33, 1–10.
- [60] Solem, J.E., Overgaard, N.C., 2005. A geometric formulation of gradient descent for variational problems with moving surfaces, in: Proceedings of International Conference on Scale-Space and PDE Methods in Computer Vision, pp. 419–430.

- [61] Szeliski, R., Scharstein, D., 2004. Sampling the disparity space image. IEEE Transactions on Pattern Analysis and Machine Intelligence 26, 419–425.
- [62] Tao, C.V., Hu, Y., 2001. A comprehensive study of the rational function model for photogrammetric processing. Photogrammetric engineering and remote sensing 67, 1347–1358.
- [63] Ummenhofer, B., Brox, T., 2015. Global, dense multiscale reconstruction for a billion points, in: Proceedings of the IEEE International Conference on Computer Vision, pp. 1341–1349.
- [64] Vu, H.H., Labatut, P., Pons, J.P., Keriven, R., 2012. High accuracy and visibility-consistent dense multiview stereo. IEEE Transactions on Pattern Analysis and Machine Intelligence 34, 889–901.
- [65] Wang, K., Frahm, J.M., 2017. Fast and accurate satellite multi-view stereo using edge-aware interpolation, in: Proceedings of International Conference on 3D Vision (3DV), pp. 365–373.
- [66] Wang, K., Stutts, C., Dunn, E., Frahm, J.M., 2016. Efficient joint stereo estimation and land usage classification for multiview satellite data, in: Proceedings of IEEE Winter Conference on Applications of Computer Vision (WACV), pp. 1–9.
- [67] Wang, M., Hu, F., Li, J., 2010. Epipolar arrangement of satellite imagery by projection trajectory simplification. The Photogrammetric Record 25, 422–436.
- [68] Wang, M., Hu, F., Li, J., 2011. Epipolar resampling of linear pushbroom satellite imagery by a new epipolarity model. ISPRS Journal of Photogrammetry and Remote Sensing 66, 347–355.
- [69] Wohlfeil, J., Hirschmüller, H., Piltz, B., Börner, A., Suppa, M., 2012. Fully automated generation of accurate digital surface models with sub-meter resolution from satellite imagery. International Archives of Photogrammetry, Remote Sensing and Spatial Information Sciences 39, 75–80.
- [70] Wrobel, B., 1987. Facets stereo vision (fast vision)—a new approach to computer stereo vision and to digital photogrammetry, in: ISPRS Intercommission Conf. Fast Processing of Photogrammetric Data, pp. 231–258.
- [71] Zach, C., Pock, T., Bischof, H., 2007. A globally optimal algorithm for robust tv-l 1 range image integration, in: Proceedings of IEEE International Conference on Computer Vision, pp. 1–8.